



# Applying Deep Embedded-Self-Organizing Map (DE-SOM) Method to Separate Geochemical Anomalous Areas of Copper-Gold Mineralization in Moalleman Region, Iran

Zohre Hoseinzade and Mohammad Hassan Bazoobandi\*

Department of Science Education, Farhangian University, P.O. Box 14665-889, Tehran, Iran

## Article Info

Received 3 September 2024

Received in Revised form 18  
September 2024

Accepted 8 November 2024

Published online 8 November 2024

DOI: [10.22044/jme.2024.15003.2861](https://doi.org/10.22044/jme.2024.15003.2861)

## Keywords

Geochemical anomaly

Deep-embedded-SOM

Batch SOM

SOM

Moalleman

## Abstract

Anomaly detection is the process of recognizing patterns in data that differ from the typical behavior. In geochemistry, this involves identifying hidden patterns and unusual components within the context of exploratory target identification. This issue is particularly significant when limited information is available about the area of interest. Therefore, employing methods that can aid in the exploration process under such conditions and with limited data is highly valuable. In this study, the Deep-Embedded Self-Organizing Map (DE-SOM), an unsupervised deep learning approach, was used to detect geochemical anomalies. The research focused on identifying multivariate geochemical anomalies in the Moalleman region. After detecting the region's geochemical anomalies, the effectiveness of the algorithm was assessed alongside two other types of SOM algorithms. For this purpose, the prediction area plot was utilized. The intersection points for DE-SOM, Batch SOM, and standard SOM were found to be 0.75, 0.67, and 0.65, respectively. The multivariate geochemical anomaly in the Moalleman area shows a good correlation with known mineral occurrences and the andesite and dacite units. Based on this, it can be stated that the DE-SOM method is a useful tool for identifying anomalies and patterns associated with mineralization.

## 1. Introduction

Anomaly detection involves identifying patterns in data that differ from what is typically expected. These unconventional patterns are commonly mentioned to as anomalies, unique features, or contaminants across various fields. Anomaly detection finds applications in a wide range of domains such as computer networks, biomedical engineering, geology, and geochemistry. For example, in geochemistry, identifying hidden patterns and anomalous components can lead to the detection of anomalies that are useful for distinguishing exploratory targets [1]. Furthermore, locating these exploratory targets is one of the most critical aspects of regional-scale geochemical exploration. In recent years, the processing of the geochemical data and the detection of anomalies associated with mineralization zones have received significant

attention [2]. The outcome of these studies has been the introduction and development of various classical and modern methods for anomaly detection, each with its own specific advantages and disadvantages [3–11].

The use of classical methods is prevalent due to their user-friendliness, lack of reliance on complex mathematics, and widespread availability [12]. However, they have certain limitations such as dependence on prior assumptions and a focus on the linear and low-order properties. Alternatively, it is well-known that the distribution of geochemical patterns is often multifaceted and complex due to intricate geological processes, posing significant challenges for classical methods [13]. Therefore, identifying geochemical anomalies requires methods capable of detecting their complex and hidden patterns link to mineralization. According



to the recent studies, artificial intelligence-based methods, which have been developed in the recent years, have shown a more effective performance in uncovering the hidden relationships between the variables. Among these, machine learning and deep learning methods have demonstrated superior effectiveness in anomaly detection compared with the traditional approaches [14–20]. Learning methods, based on the nature of the data, are generally categorized into supervised and unsupervised learning. Supervised learning relies on the labeled data, whereas unsupervised learning tackles the tasks without requiring the labeled data. Unsupervised learning is extensively applied in the areas such as feature extraction, dimensionality reduction, and clustering [13].

Clustering is fundamentally a task where the data points are grouped into homogeneous classes or clusters. Homogeneous refers to the presence of similar items within the same class, which are as similar as possible. Clustering is a popular technique for unsupervised pattern classification, dividing the input space into several regions based on certain similarity/dissimilarity criteria, so that similar elements are placed in one cluster, and dissimilar elements are grouped into separate clusters [21]. Clustering thus helps us gain an overview of the data, making it easier to detect anomalies by identifying natural patterns within the data. The core concept of employing clustering for anomaly detection involves understanding the normal patterns within the data, and then using this knowledge to determine if a data point is an outlier.

One of the clustering methods widely accepted for detecting geochemical patterns is the S-O-SOM, which is a distinct form of unsupervised learning algorithm that maps the distribution characters of input samples onto topographically organized node levels, effectively achieving clustering by reducing dimensionality [22]. SOM is distinguished from many techniques within the broader class of clustering algorithms by its inherent non-linear mapping capabilities on its low-dimensional neural surface. These advantages have led to SOM being applied in various ways including as a tool for visualizing the non-linear data relationships, conducting topology-based cluster analysis, mapping multidimensional data, and vector quantization. Additionally, in the field of geochemistry, SOM is widely used for detecting and clustering geochemical anomalies. [23,24]. For instance, in [25], the SOM algorithm was used to cluster the content of the REE samples of Fe-REE deposits of Choghart in the Bafaq region in the center of Iran (112 lithological samples). Using the

Silhouette criterion, the optimal number of clusters was determined. As a result, the studied area was divided into four zones using the self-organization map. In this work [26], the two methods of factor analysis and self-organizing maps were used to identify the geochemical associations. Although there were some differences, FA and SOM produced similar results. The findings indicate that SOM is effective in handling the variables that are not normally distributed or even categorical in nature. In study [27], to identify the geochemical anomalies in the Pangxidong area, the three methods Hierarchical clustering, Singularity mapping, and Kohonen neural network were employed. Stream sediment samples from the region were utilized in the analysis. The findings suggest that the HC method is effective for uncovering the relationships between rock-forming elements and their connection to the Ag-Au-Pb-Zn polymetallic mineralization. The SOM method highlighted the significant local variations in the enrichment and depletion. The KNN approach was useful in classifying the  $\alpha$  values of these elements, aiding in the identification of the related mineralization. A combined approach using the HC, SM, and KNN methods provides a practical strategy for identifying prospective exploration targets for undiscovered mineral reserves. In mineral potential mapping [28] adopted a hybrid approach to cluster the areas susceptible to apatite magnetite mineralization in the Esfordi sheet. The optimal number of clusters was determined using a data-driven method and a fractal model, with SOM being one of the clustering methods employed in this work.

In the aforementioned studies, SOM has often been used with satisfactory results. However, SOM is not always ideal for anomaly detection. It is well-known that due to the adaptability of SOM, its application range is quite broad, extending from image processing and biomedical engineering to robotics and pattern recognition. One of the challenges in pattern recognition is the presence of a large number of features that do not contribute to the identification of patterns. As a result, the effectiveness of learning methods is influenced by the choice of features to which they are applied. Therefore, choosing a robust algorithm for extracting effective features can significantly influence the learning outcome. Many algorithms have been developed for this purpose, with autoencoders being one of them. Autoencoders are a type of artificial neural network designed to reconstruct the input data. The primary goal of an autoencoder is to reduce the dimensionality of the

data, or compress it in a way that preserves the essential information, and then reconstruct the data using that compressed representation [17].

Considering that geochemical patterns are often complex and multifaceted due to the intricate nature of geological processes, using classical methods for feature extraction, and clustering might not produce the best results. Therefore, in this work, SOM was embedded within the layers of a deep learning algorithm to enhance its performance, and detect hidden multivariate patterns. To test the efficiency of this algorithm, both traditional and modern approaches to multivariate geochemical anomaly detection were considered. The results of the algorithm were then compared with those of SOM and Batch SOM, and validation was carried out using the prediction area plot.

## 2. Geological Setting

The Moalleman region, located in northeastern Iran in the Semnan Province, is part of the Taroud magmatic zone, and is recognized as a metallogenic province within the Central Iranian zone. This region contains numerous mineral deposits of both epithermal and hydrothermal types. These deposits include enrichments of Au, Cu, Pb, Zn, Fe, and Rare Earth Elements (REEs) [29], with the focus of this work being on copper-gold mineralization. Volcanic and intrusive rocks from the middle to late Eocene, and volcanic rocks from the Oligocene to Miocene are present in the region, which include andesitic, dacitic, and basaltic rocks. In addition, granitic masses are found in the northern part of the region [30,31]. The widespread presence of Eocene pyroclastic rocks, especially andesitic tuff and tuffs, has been reported in the studied area. Furthermore, sedimentary rocks such as limestones, marls, and shales have also been identified in the region. From an alteration perspective, the area exhibits intermediate and advanced argillic alteration, along with iron oxides, kaolinite, hectorite, hematite-limonite, alunite, and jarosite. Notably, the east-west trending Alborz Mountain range and the north-south oriented waterways, with a high stream density, suggest a relationship between clay minerals, and other sediments with felsic intrusions, particularly granitoid and volcanic rocks in the region [32].

The Moalleman region is structurally situated within the Central Iran structural zone, specifically in its northern part. This area also lies in the northern half of the Central Iran tectono-

sedimentary unit, and falls within the Central Magmatic sub-zone. The northern half of the map, known as the Torud-Chah Shirin Mountain range, is named due to its location between two major faults, the Torud and Anjilu faults, and its position along the northern edge of the Great Kavir depression. The area can be divided into two structural sub-zones: the Torud-Chah Shirin sub-zone, and the shallow Neogene sedimentary basin. The Torud-Chah Shirin sub-zone consists of Paleozoic and Mesozoic metamorphic rocks, as well as early Tertiary (Paleogene) volcanic-sedimentary deposits, which exhibit the highest magmatic activity in the region, and are primarily located in the northern half of the map. In this sub-zone, the geological structures and the general orientation of the layers trend approximately east-west, aligning relatively closely with the direction of the Torud fault zone in the region (Figure 1). This area also includes part of the Jandagh sedimentary basin, which is located in the southern portion of the map. In this basin, very shallow marine, and evaporitic deposits from the Miocene-Pliocene period are present [19,20,33,34].

## 3. Materials and Methods

### 3.1. Sampling

The regional geochemical exploration project aimed at collecting the geochemical data for the Semnan-Kashmar-Torbat Heydarieh area was executed through an agreement between a foreign geochemical-geophysical exploration company and the National Geological (NG) and mineral exploration organization's plan to enhance the quantity and quality of the geological and mineral data in the country. A systematic grid with approximate dimensions of 1.5 x 1.5 kilometers was established for sampling (Figure 2). The sampling density was set at three to four geochemical samples per 2 square kilometers. Subsequently, samples from each 2-square-kilometer area were combined to create a composite sample, which was then assigned to the center of the sampling cell. Efforts were made to collect the stream sediment samples from the headwaters during this sampling process. All samples were analyzed for 29 elements including Ag, As, Au, B, Ba, Be, Bi, Co, Cr, Cs, Cu, F, Hg, Li, Na, Nb, Mo, Ni, P, Pb, Rb, Sb, Sn, Sr, Th, U, V, W, and Zn. In the Moalleman sheet, covering an area of 1,650 square kilometers, a total of 806 composite samples were collected, resulting in a sampling density of 1.64 square kilometers per sample. These samples were analyzed using the Inductively Coupled Plasma-Mass Spectrometry (ICP-MS) technique by AMDEL (Australia) [32,33].

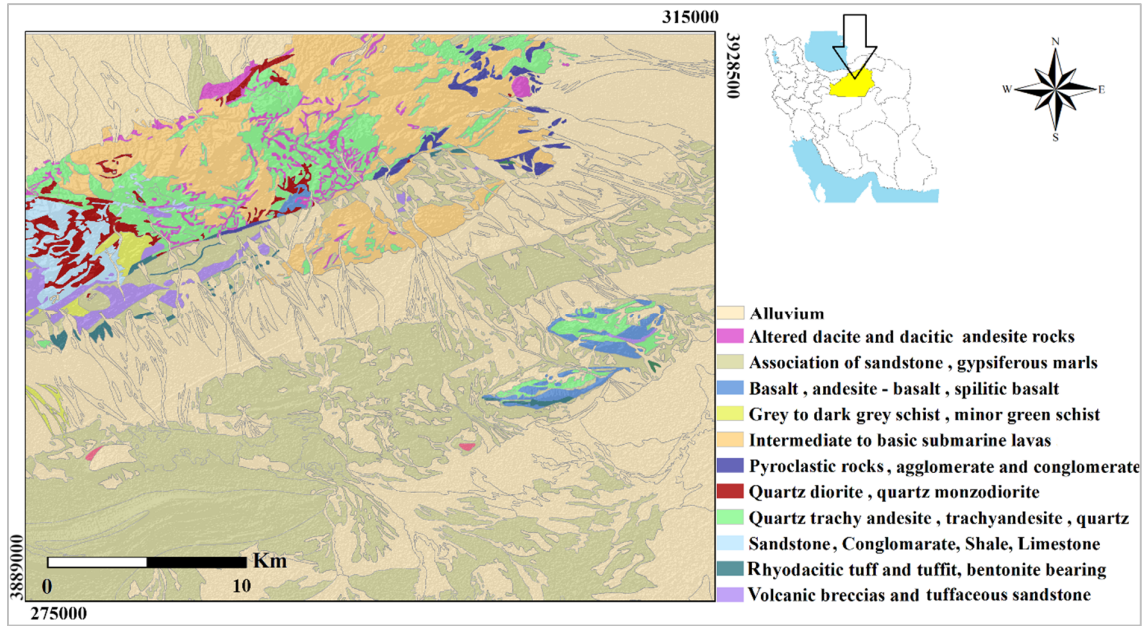


Figure 1. Geological map of the studied area.

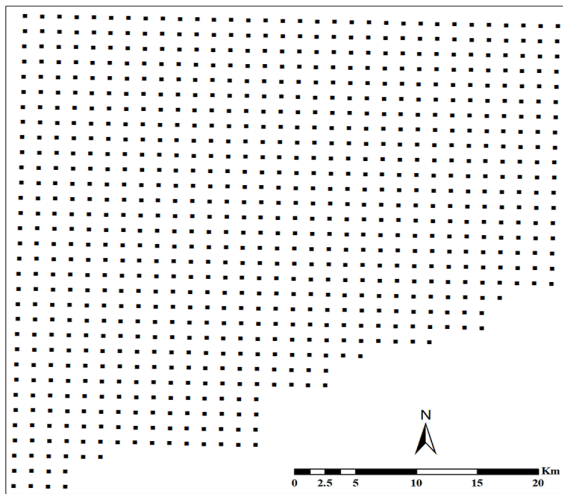


Figure 1. Sampling position in the Moalleman sheet.

### 3.2. Self-organizing map

Self-organizing neural networks, also known as the Kohonen networks, are an unsupervised method; despite their simplicity, they have demonstrated a considerable capability [22,24]. These networks are particularly useful for analyzing complex data and identifying patterns, as they can map the high-dimensional data onto a lower-dimensional space, while maintaining the topological structure of the original data. The structure of a self-organizing network consists of two layers (input and output). The output layer is typically organized as a 2D grid of neurons, similar to a matrix. Each neuron in the output layer is associated with a weight vector. The neurons are

arranged in such a way that their neighborhood relationships in the output grid reflect their neighborhood relationships in the input data space. The training process involves presenting the input data to the network [22,24]. For each input data point, the neuron whose weight vector most closely matches the input data is selected as the "winning" neuron. In the following step, the weights of the winning, and its neighboring neurons are adjusted to move the closer to the input data. This process was repeated for all the training data. By iteratively adjusting the weights in this manner, the network learns to represent the input data's topological relationships in a lower-dimensional output space, making it a powerful tool for pattern recognition and data analysis [22].

The collection of the input data samples is shown by  $X = \{x_i\} | 1 \leq i \leq N$ , where  $x_i \in RD$ . A SOM is made up of  $K$  units, each linked to a group of prototype vectors  $\{m_k\} | 1 \leq k \leq K$ . In a typical SOM, the prototype vectors are located within the same space as the input data, i.e.  $RD$ . A data point is assigned to the nearest prototype vector on the map based on the Euclidean distance [35]. The corresponding map unit is referred to as the BMU [35]. The BMU is defined as the point  $x_i$  by  $b_i$ :

$$b_i = \underset{k}{\operatorname{argmin}} \|x_i - m_k\|_2^2 \quad (1)$$

The network topology enables the determination of distances between various units,  $\delta(k,l)$ . The topological distance between units  $k$  and  $l$  on the map is represented, and typically measured using the Manhattan distance, which is the shortest

path between the two units on the map. The neighborhood function of the map is defined, and a temperature parameter ( $T$ ) is introduced, which determines the size of the neighborhood area surrounding a unit [35]. In this work, a Gaussian neighborhood function was employed, which was described as follows:

$$\kappa^T(d) = e^{-\frac{d^2}{T^2}} \quad (2)$$

The basic SOM algorithm, often referred to as the Kohonen algorithm, processes each training point  $x_i$  by adjusting each prototype vector to move it closer to  $x_i$ . These adjustments are weighted according to the neighborhood around the BMU, with neighboring units experiencing substantial changes, while units farther away remain

unchanged [35]. This is expressed by the following formula:

$$\mathbf{m}_k \leftarrow \mathbf{m}_k + \alpha \kappa^T(\delta(b_i, k))(\mathbf{x}_i - \mathbf{m}_k) \quad (3)$$

In the above equation,  $\alpha$  represents a learning rate that decreases over the course of training. One of the disadvantages of this algorithm is its slow convergence; it is sequential, and cannot be performed in parallel. To address this issue, a variant called Batch SOM was developed, which processed all the data points in a batch. This allows for a faster training, and often leads to better results, especially for large datasets [35]. The Batch SOM algorithm involves minimizing the following cost function, known as the distortion measure:

$$\mathcal{L}_{SOM}(\{\mathbf{m}_k\}, \mathbb{X}, b, T) = \frac{1}{N} \sum_{i=1}^N \sum_{k=1}^K \kappa^T(\delta(b_i, k)) \|\mathbf{x}_i - \mathbf{m}_k\|_2^2 \quad (4)$$

The distortion caused by BMU assignments is not directly differentiable [35]. Nonetheless, this can be empirically reduced through a dynamic clustering approach akin to k-means, which cycles between two main steps: assigning best matching units, and minimizing distortion [35].

$$\mathbf{m}_k \leftarrow \frac{\sum_{l=1}^K \kappa^T(\delta(k, l)) \sum_{i=1}^N \mathbb{1}_{[b_i=l]} \mathbf{x}_i}{\sum_{l=1}^K \kappa^T(\delta(k, l)) \sum_{i=1}^N \mathbb{1}_{[b_i=l]}} \quad (5)$$

### 3.3. Deep self-organizing map

The structure of the Deep SOM model is built around three primary elements: an encoder, a SOM layer, and a decoder. The encoder maps the input data to a latent intermediate space. Training of the SOM occurs within this latent space, using the encoded data. Following this, the decoder works to transform the latent codes back to the original input space, with the goal of precisely reconstructing the

inputs [35]. Detailed descriptions of each component will be provided in the subsequent sections.

#### 3.3.1 Loss function

The weights of the encoder and decoder parameters are denoted by  $W_e$  and  $W_d$ , respectively. The encoding function is represented by  $f_{w_e}$  and the decoding function by  $g_{w_d}$  [29]. Therefore,  $z_i = f_{w_e}(x_i) \in R^L$  is the encoded version of  $x_i$  in the latent space, and  $\tilde{x}_i = g_{w_d}(f_{w_e}(x_i)) \in R^D$ ; it is the decoder's reconstruction. Our goal was to simultaneously improve the weights of the autoencoder network and the prototype vectors of the SOM [35]. To achieve this, a hybrid loss function was defined, consisting of two components, as expressed below:

$$\mathcal{L}(W_e, W_d, \mathbf{m}_1, \dots, \mathbf{m}_K) = \mathcal{L}_R(W_e, W_d) + \gamma \mathcal{L}_{SOM}(W_e, \mathbf{m}_1, \dots, \mathbf{m}_K) \quad (6)$$

The first component,  $\mathcal{L}_R$ , is the reconstruction loss of the autoencoder. The Mean Squared Error (MSE) loss is used, which is equivalent to the negative log-likelihood of a Gaussian distribution centered on the reconstruction.

$$\mathcal{L}_R = \frac{1}{N} \sum_{i=1}^N \mathcal{L}_R^i = \frac{1}{N} \sum_i \|\tilde{x}_i - x_i\|_2^2 \quad (7)$$

The second component of the loss is related to the SOM, and is denoted by  $\mathcal{L}_{SOM}$ . This loss relies on a set of parameters  $\{\mathbf{m}_k\}_{1 \leq k \leq K}$  and the BMUs, which assign a latent data point to the nearest prototype based on the Euclidean distance [35]:

$$b_i = \underset{k}{\operatorname{argmin}} \|\mathbf{z}_i - \mathbf{m}_k\|_2^2 \quad (8)$$

The loss function for the self-organizing map is expressed as follows:

$$\mathcal{L}_{SOM} = \frac{1}{N} \sum_{i=1}^N \mathcal{L}_{SOM}^i = \frac{1}{N} \sum_i \sum_{k=1}^K \kappa^T(\delta(b_i, k)) \|z_i - \mathbf{m}_k\|_2^2 \quad (9)$$

The coefficient  $\gamma$  is a hyperparameter that balances the minimization of the autoencoder's reconstruction error and the SOM error. Therefore, the SOM loss functions as a SOM-guided regularizer [35].

### 3.3.2. Interpretation of topological organization

The SOM loss can be separated into two components: the first component is the squared distance between the BMU and the latent point, while the second component pertains to the topological relationship with neighboring units [35].

$$\begin{aligned} \mathcal{L}_{SOM} &= \frac{1}{N} \sum_{i=1}^N \sum_{k=1}^K \kappa^T(\delta(b_i, k)) \|z_i - \mathbf{m}_k\|_2^2 = \frac{1}{N} \sum_{i=1}^N \left[ \kappa^T(\delta(b_i, b_i)) \|z_i - \mathbf{m}_{b_i}\|_2^2 + \sum_{k \neq b_i} \kappa^T(\delta(b_i, k)) \|z_i - \mathbf{m}_k\|_2^2 \right] \\ &= \frac{1}{N} \sum_{i=1}^N \|z_i - \mathbf{m}_{b_i}\|_2^2 + \frac{1}{N} \sum_{i=1}^N \sum_{k \neq b_i} \kappa^T(\delta(b_i, k)) \|z_i - \mathbf{m}_k\|_2^2 \end{aligned} \quad (12)$$

For large values of T, the second component dominates, resulting in a topological organization. As the temperature decreases towards zero, the first component takes precedence, making the SOM loss resemble the k-means loss [35], where the centroids correspond to the prototypes of the map.

$$\lim_{T \rightarrow 0} \mathcal{L}_{SOM} = \frac{1}{N} \sum_i \|z_i - \mathbf{m}_{b_i}\|_2^2 = \mathcal{L}_{k\text{-means}} \quad (12)$$

Therefore, as the temperature approaches zero, the hybrid loss function can be written as follows:

$$\lim_{T \rightarrow 0} \mathcal{L} = \mathcal{L}_R + \gamma \mathcal{L}_{k\text{-means}} \quad (12)$$

### 3.3.3. Training method

A joint training method was employed, where the network parameters and prototypes were optimized using back-propagation and stochastic gradient descent. The assignments to the BMUs were kept fixed between each optimization step, as they are not differentiable. Therefore, the weight coefficients  $w_{i,k} \equiv \kappa^T(\delta(b_i, k))$  simplify to fixed coefficients for each data point and prototype, given the network parameters and prototypes. The gradients of the loss function with respect to the autoencoder weights and prototypes are easily obtained when the assignments are considered fixed at each step [35].

$$\frac{\partial \mathcal{L}}{\partial \mathbf{W}_e} = \frac{\partial \mathcal{L}_R}{\partial \mathbf{W}_e} + \gamma \frac{\partial \mathcal{L}_{SOM}}{\partial \mathbf{W}_e} \quad (13)$$

$$\frac{\partial \mathcal{L}}{\partial \mathbf{W}_d} = \frac{\partial \mathcal{L}_R}{\partial \mathbf{W}_d}$$

$$\frac{\partial \mathcal{L}}{\partial \mathbf{m}_k} = \gamma \frac{\partial \mathcal{L}_{SOM}}{\partial \mathbf{m}_k}$$

The gradients for a data point  $x_i$  are given as follows:

$$\begin{aligned} \frac{\partial \mathcal{L}_R^i}{\partial \mathbf{W}_e} &= 2(\mathbf{g}_{\mathbf{W}_d}(\mathbf{f}_{\mathbf{W}_e}(x_i)) - x_i) \frac{\partial \mathbf{g}_{\mathbf{W}_d}(\mathbf{f}_{\mathbf{W}_e}(x_i))}{\partial \mathbf{W}_e} \\ \frac{\partial \mathcal{L}_R^i}{\partial \mathbf{W}_d} &= 2(\mathbf{g}_{\mathbf{W}_d}(\mathbf{f}_{\mathbf{W}_e}(x_i)) - x_i) \frac{\partial \mathbf{g}_{\mathbf{W}_d}(\mathbf{f}_{\mathbf{W}_e}(x_i))}{\partial \mathbf{W}_d} \end{aligned} \quad (14)$$

$$\frac{\partial \mathcal{L}_{SOM}^i}{\partial \mathbf{W}_e} = 2 \sum_{k=1}^K w_{i,k} (\mathbf{f}_{\mathbf{W}_e}(x_i) - \mathbf{m}_k) \frac{\partial \mathbf{f}_{\mathbf{W}_e}(x_i)}{\partial \mathbf{W}_e}$$

$$\frac{\partial \mathcal{L}_{SOM}^i}{\partial \mathbf{m}_k} = 2w_{i,k} (\mathbf{m}_k - \mathbf{f}_{\mathbf{W}_e}(x_i))$$

Batch gradient descent is not effective for large datasets, as it can result in a slow convergence. Conversely, using a batch size of one, as in the stochastic Kohonen algorithm, would be inefficient for training the autoencoder, and would particularly fail to take advantage of parallel implementations [35]. Considering a batch B of  $n_b$  samples, the encoder weights are updated as follows:

$$\mathbf{W}_e \leftarrow \mathbf{W}_e - \frac{l_r}{n_b} \sum_{i \in B} \left( \frac{\partial \mathcal{L}_R^i}{\partial \mathbf{W}_e} + \gamma \frac{\partial \mathcal{L}_{SOM}^i}{\partial \mathbf{W}_e} \right) \quad (15)$$

The decoder weights are updated as follows:

$$\mathbf{W}_d \leftarrow \mathbf{W}_d - \frac{l_r}{n_b} \sum_{i \in \mathcal{B}} \frac{\partial \mathcal{L}_R^i}{\partial \mathbf{W}_d} \quad (16)$$

and finally, the map prototypes are updated using the following update rule:

$$\mathbf{m}_k \leftarrow \mathbf{m}_k - \frac{l_r}{n_b} \sum_{i \in \mathcal{B}} \gamma \frac{\partial \mathcal{L}_{SOM}^i}{\partial \mathbf{m}_k} \quad (17)$$

By expanding the prototype update rule in Equation 17, we arrive at an expression that can be considered a middle ground between the stochastic the SOM and Batch SOM algorithms, which we can referred to as a mini-batch SOM:

$$\mathbf{m}_k \leftarrow \mathbf{m}_k + 2\gamma \frac{l_r}{n_b} \sum_{i \in \mathcal{B}} \kappa^T(\delta(b_i, k))(\mathbf{z}_i - \mathbf{m}_k) \quad (18)$$

Similar to Batch SOM, we alternated between BMU assignments and minimization. However, the minimization was performed using a gradient descent step, much like in stochastic SOM [35].

#### 4. Preparation of Input Layers

Given the target mineralization in this work, it is essential to identify the appropriate elements for

detecting geochemical anomalies. For this purpose, factor analysis, a multivariate method, was utilized. Factor analysis is a technique that analyzes the variance between several dependent variables by describing them in terms of a few latent variables. In other words, this method aims to simplify a complex data by describing it using a smaller number of variables. This technique and its variations have been widely used in geochemical studies and mineral potential modeling [36-41]. In this work, simple factor analysis was employed to uncover the hidden relationships between elements. The loadings associated with the factors are recorded in Table 1. Based on the results of the factor analysis, the highest loadings in Factor 1 were assigned to the elements Cu, Co, V, Rb, Sr, and P. In Factor 2, the elements Pb, Zn, Ag, Sb, and Hg had the highest loadings. In Factor 3, Au, B, W, and Bi showed the highest coefficients. Due to their genetic association with mineralization, high mobility in hydrothermal fluids, and stability in surface environments, the presence of high loadings for key elements such as Cu, Au, and As is significant. Accordingly, the factors associated with these elements were selected for algorithm implementation.

**Table 1. Loading of factor analysis.**

| Elements | D1     | D2     | D3     | D4     | D5     |
|----------|--------|--------|--------|--------|--------|
| zn       | 0.254  | 0.841  | 0.032  | 0.071  | 0.167  |
| pb       | -0.010 | 0.893  | 0.218  | -0.025 | 0.067  |
| ag       | -0.147 | 0.784  | 0.190  | -0.020 | -0.143 |
| cr       | 0.430  | -0.123 | -0.010 | 0.641  | 0.134  |
| ni       | 0.061  | -0.005 | 0.164  | 0.814  | 0.018  |
| bi       | 0.190  | 0.189  | 0.808  | -0.091 | 0.140  |
| cu       | 0.691  | 0.135  | 0.399  | 0.148  | -0.204 |
| as       | 0.031  | 0.532  | 0.036  | 0.192  | 0.179  |
| sb       | 0.219  | 0.786  | 0.083  | -0.156 | 0.120  |
| co       | 0.760  | 0.127  | 0.222  | 0.400  | 0.044  |
| sn       | 0.056  | -0.122 | 0.312  | 0.272  | 0.484  |
| ba       | -0.275 | 0.574  | -0.115 | 0.129  | -0.026 |
| v        | 0.815  | -0.088 | -0.117 | 0.130  | 0.064  |
| sr       | -0.754 | -0.079 | -0.056 | 0.172  | -0.181 |
| hg       | -0.085 | 0.856  | 0.069  | -0.025 | 0.006  |
| w        | 0.252  | 0.112  | 0.623  | -0.018 | 0.550  |
| b        | -0.088 | 0.015  | 0.711  | 0.256  | 0.378  |
| be       | 0.560  | 0.069  | 0.314  | 0.113  | 0.593  |
| mo       | -0.283 | 0.340  | 0.555  | -0.057 | 0.317  |
| li       | 0.239  | -0.010 | -0.135 | 0.621  | 0.216  |
| au       | 0.254  | 0.395  | 0.681  | 0.072  | -0.100 |
| rb       | 0.604  | 0.073  | 0.172  | 0.004  | 0.617  |
| p        | 0.880  | -0.043 | -0.027 | 0.100  | 0.186  |
| cs       | 0.499  | 0.050  | -0.088 | 0.491  | 0.060  |
| nb       | 0.236  | 0.132  | 0.088  | 0.090  | 0.782  |
| th       | -0.267 | 0.017  | 0.432  | 0.142  | 0.366  |
| u        | -0.032 | 0.049  | 0.116  | 0.053  | 0.823  |

## 5. Results and Assessment

The use of an appropriate algorithm to identify geochemical anomalies is essential due to the geological complexities of the studied area. Therefore, a deep unsupervised learning algorithm called Deep Embedded SOM was employed. This algorithm utilizes three neural network modules, each responsible for a specific task. Initially, the input is transferred to an intermediate latent space by the encoder. In this space, the SOM is trained, and receives the encoded inputs. Then the latent code is returned to the original space by the decoder. At this stage, the goal is to accurately reconstruct the inputs. The model is trained for a specified number of iterations until the error converges. During each iteration, the weights of the autoencoder and the prototypes of the SOM are updated.

After the implementation of the algorithm, the weight assigned to each cluster is determined using the prediction area plot, and the anomalous clusters are separated from the background. This plot contains two curves, one of which is related to the prediction rate of mineral occurrences known by each class, and the other is the percentage of the area occupied by each class. In fact, these curves serve as a criteria for evaluating the classes of a geochemical model. In the p-a plot of a model, if the intersection point shows a higher value compared with the p-a plot of other models; it means that it has the lowest percentage of the area covered. As a result, this model will have the most weight, because the sum of the prediction rate and the occupied area for the intersection point is equal to 100. To assign quantitative weights to the clusters, first the normalized density is calculated. The normalized density is used to rank the clusters. To determine the normalized density using the parameters of P-A plot, the ratio of the prediction

rate to the occupied area at the intersection point was calculated [42].

The mentioned algorithm was implemented on the geochemical data in the studied area. Then, using the weight assigned to each cluster, the regions with different degrees were separated from each other (Table 2). In the next step, according to the obtained weights, the clusters are classified into three general categories: anomaly, halo, and background, and the results of all the three SOM, Batch SOM, and Deep Embedded SOM algorithms are presented in Figure 3. According to the maps, the SOM algorithm has introduced a large part of the studied area under the title of anomaly. Meanwhile, Deep Embedded SOM considers a smaller area as an anomaly, and this shows the effective performance of the algorithm.

One of the suitable methods for evaluating the results obtained from the applied techniques, and assessing their effectiveness in identifying the desired anomaly is the use of the ROC curve to examine the sensitivity of the method. Sensitivity refers to the ratio of correctly classified cells to incorrectly classified ones. Various methods have been developed for this purpose including different evaluation curves and parameters such as accuracy and sensitivity. One of the most recent methods introduced in this area is the Prediction-Area (P-A) plot, introduced by [42], and it has been widely used in many studies [43–46]. Finally, based on the anomaly models, the number of high-potential points predicted in each class and the corresponding class areas, P-A plots were generated. According to Figure 4, in the generated geochemical anomaly model, 75% of the known mineral occurrences were predicted in about 25% of the studied area using the Deep Embedded SOM method, 65% in approximately 35% of the studied area using the Batch SOM method, and 67% in about 33% using the SOM method.

**Table 2. Prediction rate and area for each class in SOM, Batch SOM, and Deep SOM.**

| Methods   | Class | Area  | Prediction rate | Weight |
|-----------|-------|-------|-----------------|--------|
| SOM       | 1     | 31.19 | 68              | 0.33   |
|           | 2     | 14.59 | 0               | -      |
|           | 3     | 54.22 | 32              | -0.22  |
| Batch SOM | 1     | 26.62 | 64              | 0.38   |
|           | 2     | 12.8  | 0               | -      |
|           | 3     | 60.57 | 36              | -0.22  |
| Deep SOM  | 1     | 13.13 | 55              | 0.62   |
|           | 2     | 29.63 | 33              | 0.04   |
|           | 3     | 57.24 | 12              | -0.67  |

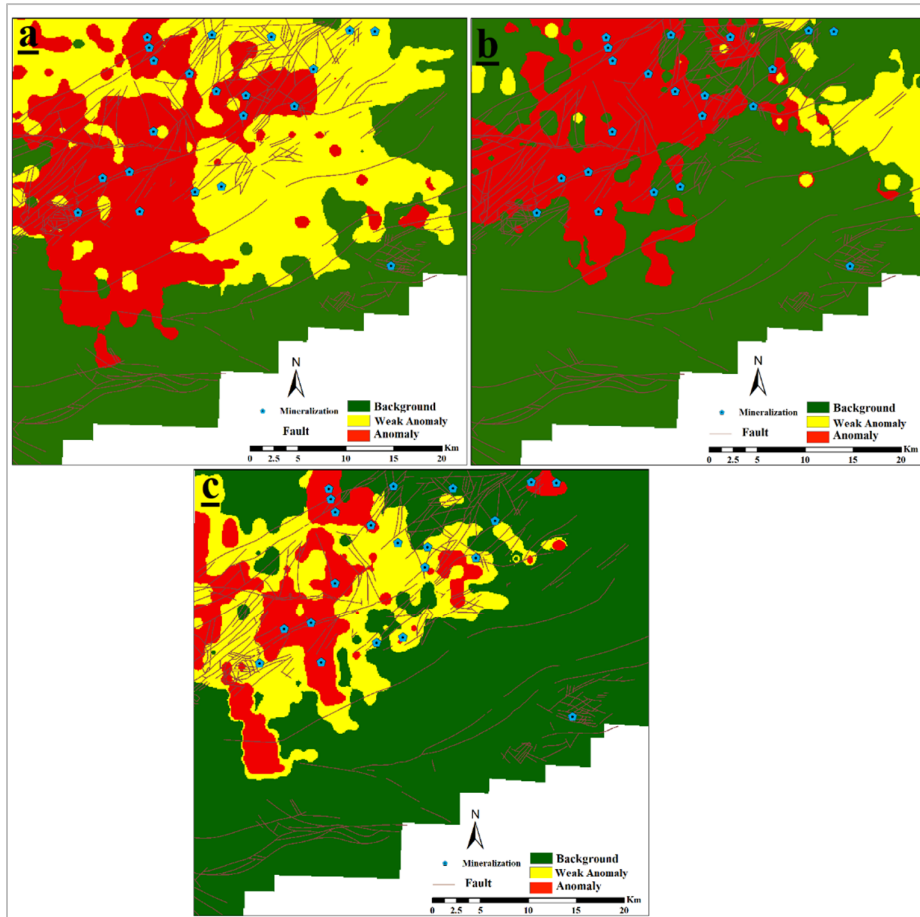


Figure 2. Multivariate geochemical map in the studied area. a) SOM. b) Batch SOM. c) Deep-embedded SOM.

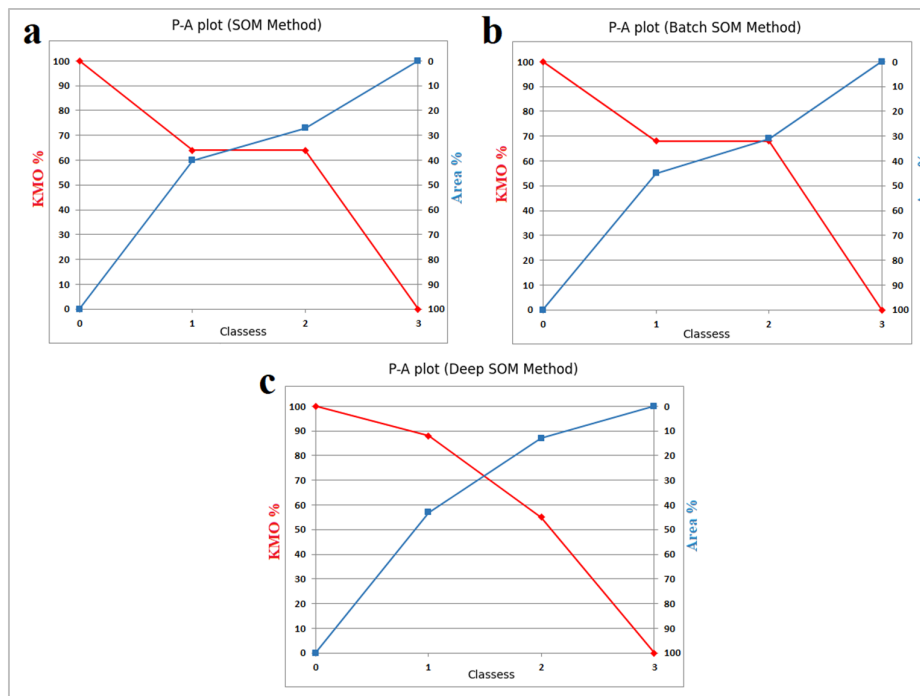


Figure 3. Prediction area plot. a) SOM. b) Batch SOM. c) Deep-embedded SOM.

## 6. Conclusions

Clustering and classification are among the most important and fundamental issues in data analysis, data mining, and machine learning. These two methods allow us to uncover hidden structures, patterns, and relationships in the data, enabling effective decision-making and prediction. Data learning, whether supervised or unsupervised, is inherently associated with uncertainty. This is primarily because learning as generalization beyond the observed data, is necessarily based on an inductive inference process. Inductive inference replaces specific observations with general models that describe the data generation process. However, these models are always hypothetical and, as a result, come with uncertainty. In fact, the observed data can generally be explained by more than one theory or model. This means that we can never be certain of the accuracy of a particular model and its predictions, marking the onset of uncertainty. This uncertainty in machine learning can arise from various factors such as noise in the data, sampling limitations, and the inherent complexity of the systems under study.

According to Figure 3, it was observed that with a change in the method, the position of geochemical anomalies is shifted, and the three different methods produced varying extents of anomalies in the Moalleman region. This is natural, as each of the three methods has different structures and assumptions, and they perform clustering based on various algorithms and criteria. This means that the choice of model introduces varying degrees of uncertainty. Therefore, a method must be used to reduce uncertainty in the final outcome. Several methods exist to achieve a more reliable model including model combination techniques, cross-validation, and uncertainty quantification [47–49]. These methods aim to improve accuracy and reduce uncertainty by combining the results of different models or evaluating them based on specific criteria. In this work, the maximin method was used to create a combined model with a high confidence level. This method, used in decision theory and statistics, serves as a cautious strategy in the face of uncertainty and risk. The maximin method works by selecting the option that provides the best outcome in the worst-case scenario, in situations where the results of decisions are uncertain or dependent on complex conditions. In other words, this method seeks to minimize the maximum possible loss. The method follows a cautious strategy, where the decision-maker selects an option that offers the best result in the worst

possible conditions [50]. The resulting map is presented in Figure 5, which shows that the results of the other methods are well-supported, and more reliable targets are produced. This method reduces uncertainty by combining the results of different models and selecting the output with the highest agreement among the models. This approach can be particularly useful in situations where models perform variably. It is important to note here that the combined model does not necessarily outperform individual models in all cases. Some models require parameters that must be correctly adjusted [48]. If these parameters are not properly set, the performance of the combined model may be affected. Additionally, the combining models can increase computational complexity, and require more resources. Therefore, while the combined methods can help reduce uncertainty and improve accuracy, they should be applied carefully, considering the characteristics of the models used and the need for an appropriate parameter tuning. The selection of suitable models for combination and the correct adjustment of parameters are crucial for achieving optimal results.

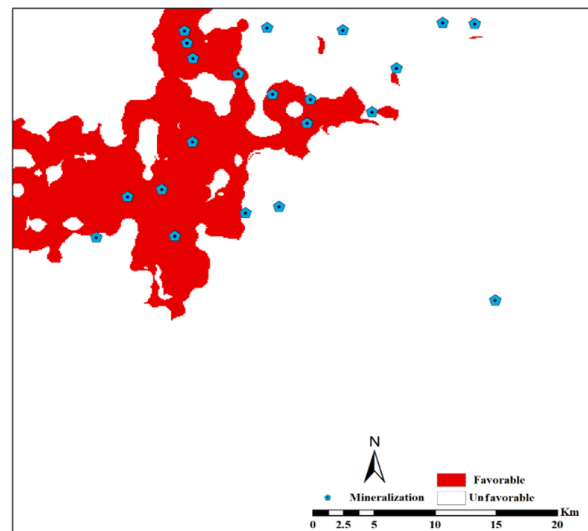


**Figure 4. Delineation of geochemical anomalies based on the maximin scores**

## Acknowledgment

We would like to thank the research and technology council of Farhangian University for financial support through this investigation under post doctorate project No. 50000/17337/600

## References

- [1] Zekri, H., Mokhtari, A.R. and Cohen, D.R. (2019). Geochemical pattern recognition through matrix

- decomposition. *Ore Geology Reviews*, 104, 670-685. <https://doi.org/10.1016/j.oregeorev.2018.11.026>
- [2] Shahrestani, S. and Mokhtari, A.R. (2017). Improved detection of anomalous catchment basins by incorporating drainage density in dilution correction of geochemical residuals. *Geochemistry: Exploration, Environment, Analysis*, 17(3), 194-203. <https://doi.org/10.1144/geochem2016-015>
- [3] Hoseinzade, Z., Mokhtari, A.R. and Zekri, H. (2018). Application of radial basis function in the analysis of irregular geochemical patterns through spectrum-area method. *Journal of Geochemical Exploration*, 194, 257-265. <https://doi.org/10.1016/j.gexplo.2018.09.002>
- [4] Shahrestani, S. and Mokhtari, A.R. (2017). Dilution correction equation revisited: The impact of stream slope, relief ratio and area size of basin on geochemical anomalies. *Journal of African Earth Sciences*, 128, 16-26. <https://doi.org/10.1016/j.jafrearsci.2016.06.019>
- [5] Hosseini, S.A., Khah, N.K.F., Kianoush, P., Afzal, P., Ebrahimabadi, A. and Shirinabadi, R. (2023). Integration of fractal modeling and correspondence analysis reconnaissance for geochemically high-potential promising areas, NE Iran. *Results in Geochemistry*, 11, 100026. <https://doi.org/10.1016/j.ringeo.2023.100026>
- [6] Afzal, P., Khakzad, A., Moarefvand, P., Omran, N.R., Esfandiari, B. and Alghalandis, Y.F. (2010). Geochemical anomaly separation by multifractal modeling in Kahang (Gor Gor) porphyry system, Central Iran. *Journal of Geochemical Exploration*, 104(1-2), 34-46. <https://doi.org/10.1016/j.gexplo.2009.11.003>
- [7] Yousefi, M. (2017). Analysis of Zoning Pattern of Geochemical Indicators for Targeting of Porphyry-Cu Mineralization: A Pixel-Based Mapping Approach. *Natural Resources Research*, 26, 429-441. <https://doi.org/10.1007/s11053-017-9334-7>
- [8] Yousefi, M. (2017). Recognition of an enhanced multi-element geochemical signature of porphyry copper deposits for vectoring into mineralized zones and delimiting exploration targets in Jiroft area, SE Iran. *Ore Geology Reviews*, 83, 200-214. <https://doi.org/10.1016/j.oregeorev.2016.12.024>
- [9] Mahdianfar, H. and Seyedrahimi-Niarraq, M. (2022). Improvement of geochemical prospectivity mapping using power spectrum-area fractal modelling of the multi-element mineralization factor (SAF-MF). *Geochemistry: Exploration, Environment, Analysis*, 22(4), geochem2022-015. <https://doi.org/10.1144/geochem2022-015>
- [10] Seyedrahimi-Niarraq, M., Mahdianfar, H. and Mokhtari, A.R. (2023). Application of geochemical structural methods to determine lead-contaminated areas related to mining activities. *Journal of Analytical and Numerical Methods in Mining Engineering*, 13(34), 41-55. <https://doi.org/10.22034/ANM.2022.2783>
- [11] Mahdianfar, H. and Niarraq, M.S. (2023). Integration of Fractal and Multivariate Principal Component Models for Separating Pb-Zn Mineral Contaminated Areas. *Journal of Mining and Environment*, 14(3), 1019-1035. <https://doi.org/10.22044/jme.2023.13227.2424>
- [12] Hoseinzade, Z. and Mokhtari, A.R. (2017). A comparison study on detection of key geochemical variables and factors through three different types of factor analysis. *Journal of African Earth Sciences*, 134, 557-563. <https://doi.org/10.1016/j.jafrearsci.2017.07.025>
- [13] Zuo, R., Xiong, Y., Wang, J. and Carranza, E.J.M. (2019). Deep learning and its application in geochemical mapping. *Earth Sci Rev*, 192, 1-14. <https://doi.org/10.1016/j.earscirev.2019.02.023>
- [14] Farhadi, S., Tatullo, S., Boveiri Konari, M. and Afzal, P. (2024). Evaluating StackingC and ensemble models for enhanced lithological classification in geological mapping. *Journal of Geochemical Exploration*, 260, 107441. <https://doi.org/10.1016/j.gexplo.2024.107441>
- [15] Pourgholam, M.M., Afzal, P., Adib, A., Rahbar, K. and Gholinejad, M. (2024). Recognition of REEs anomalies using an image Fusion fractal-wavelet model in Tarom metallogenic zone, NW Iran. *Geochemistry*, 84(2), 126093. <https://doi.org/10.1016/j.chemer.2024.126093>
- [16] Afzal, P., Farhadi, S., Konari, M.B., Meigoony, M.S. and Saein, L.D. (2022). Geochemical anomaly detection in the Irankuh District using Hybrid Machine learning technique and fractal modeling. *Geopersia*, 12(1), 191-199. <https://doi.org/10.22059/GEOPE.2022.336072.648644>
- [17] Soltani, Z., Hassani, H. and Esmaeiloghli, S. (2024). A deep autoencoder network connected to geographical random forest for spatially aware geochemical anomaly detection. *Computers & Geosciences, Pergamon*, 190, 105657. <https://doi.org/10.1016/J.CAGEO.2024.105657>
- [18] Saremi, M., Bagheri, M., Agha Seyyed Mirzabozorg, S.A., Hassan, N.E., Hoseinzade, Z., Maghsoudi, A. et al. (2024). Evaluation of Deep Isolation Forest (DIF) Algorithm for Mineral Prospectivity Mapping of Polymetallic Deposits. *Minerals*, Vol 14, Page 1015, *Multidisciplinary Digital Publishing Institute*, 14, 1015. <https://doi.org/10.3390/MIN14101015>
- [19] Esmaeiloghli, S., Tabatabaei, S.H. and Carranza, E.J.M. (2023). Empirical mode decomposition and power spectrum filtering for detection of frequency channels related to multi-scale geochemical anomalies: Metal exploration targeting in Moalleman district, NE Iran. *Journal of Geochemical*

- Exploration, Elsevier*, 246, 107157. <https://doi.org/10.1016/J.GEXPLO.2023.107157>
- [20] Esmailoghli, S., Tabatabaei, S.H. and Carranza, E.J.M. (2023). Infomax-based deep autoencoder network for recognition of multi-element geochemical anomalies linked to mineralization. *Computers & Geosciences, Pergamon*, 175, 105341. <https://doi.org/10.1016/J.CAGEO.2023.105341>
- [21] Abedi, M., Norouzi, G.H. and Torabi, S.A. (2013). Clustering of mineral prospectivity area as an unsupervised classification approach to explore copper deposit. *Arabian Journal of Geosciences*, 6, 3601-3613. <https://doi.org/10.1007/s12517-012-0615-5>
- [22] Kohonen, T. (2012). Self-organization and associative memory (Vol. 8). *Springer Science & Business Media*.
- [23] Kohonen, T. (1997, June). Exploration of very large databases by self-organizing maps. In *Proceedings of international conference on neural networks (icnn'97) (Vol. 1, pp. PL1-PL6)*. IEEE.
- [24] Kohonen, T., (1990). The self-organizing map. *Proc IEEE* 78, 1464-1480,
- [25] Sarparandeh, M. and Hezarkhani, A. (2016). Application of Self-Organizing Map for Exploration of REEs' Deposition. *Open Journal of Geology*, 6(07), 571. <https://doi.org/10.4236/ojg.2016.67045>
- [26] Žibret, G. and Šajn, R. (2010). Hunting for geochemical associations of elements: Factor analysis and self-organising maps. *Mathematical Geosciences*, 42, 681-703. <https://doi.org/10.1007/s11004-010-9288-3>
- [27] Yu, X., Xiao, F., Zhou, Y., Wang, Y. and Wang, K. (2019). Application of hierarchical clustering, singularity mapping, and Kohonen neural network to identify Ag-Au-Pb-Zn polymetallic mineralization associated geochemical anomaly in Pangxidong district. *Journal of Geochemical Exploration, Elsevier*, 203, 87-95. <https://doi.org/10.1016/J.GEXPLO.2019.04.007>
- [28] Mirzabozorg, S.A.A.S., Abedi, M. and Ahmadi, F. (2023). Clustering of Areas Prone to Iron Mineralization in Esfordi Range based on a Hybrid Method of Knowledge- and Data-Driven Approaches. *Journal of Mineral Resources Engineering*, 8(4): 1-26,
- [29] Modabberi, S., Ahmadi, A. and Tangestani, M.H. (2017). Sub-pixel mapping of alunite and jarosite using ASTER data; a case study from north of Semnan, north central Iran. *Ore Geology Reviews*, 80, 429-436. <https://doi.org/10.1016/j.oregeorev.2016.07.014>
- [30] Yousefi, F., Sadeghian, M., Wanhainen, C., Ghasemi, H. and Frei, D. (2017). Geochemistry, petrogenesis and tectonic setting of middle Eocene hypabyssal rocks of the Torud-Ahmad Abad magmatic belt: An implication for evolution of the northern branch of Neo-Tethys Ocean in Iran. *Journal of Geochemical Exploration*, 178, 1-15. <https://doi.org/10.1016/j.gexplo.2017.03.008>
- [31] Haghypour, A.S.A., (1985). Geological Map of Iran.
- [32] Torshizian, H., Afzal, P., Rahbar, K., Yasrebi, A.B., Wetherelt, A. and Fyzollahi, N. (2021). Application of modified wavelet and fractal modeling for detection of geochemical anomaly. *Geochemistry, 81*. <https://doi.org/10.1016/j.chemer.2021.125800>
- [33] Esmailoghli, S., Lima, A. and Sadeghi, B. (2024). Lithium exploration targeting through robust variable selection and deep anomaly detection: An integrated application of sparse principal component analysis and stacked autoencoders. *Geochemistry, Urban & Fischer*, 126111. <https://doi.org/10.1016/J.CHEMER.2024.126111>
- [34] Mohamadi, Z., Ziaii, M. and Ziaii, M. (2018). Application of PCA method for hydrothermal alteration mapping in the Torud (Shahrood) area based on ASTER and Sentinel-2A multispectral data. *The 36th National and the 3rd International Geosciences Congress of Iran, Tehran, Iran*,
- [35] Forest, F., Lebbah, M., Azzag, H. and Lacaille, J. (2021). Deep embedded self-organizing maps for joint representation learning and topology-preserving clustering. *Neural Computing and Applications*, 33. <https://doi.org/10.1007/s00521-021-06331-w>
- [36] Yousefi, M., M.M., G.S.E., G.S., & D.S.L. (2019). Delineation of podiform-type chromite mineralization using geochemical mineralization prospectivity index and staged factor analysis in Balvard area (SE Iran). *J Min Environ*, 10, 705-15.
- [37] Afzal, P., Mirzaei, M., Yousefi, M., Adib, A., Khalajmasoumi, M., Zarifi, A.Z. et al. (2016). Delineation of geochemical anomalies based on stream sediment data utilizing fractal modeling and staged factor analysis. *Journal of African Earth Sciences*, 119, 139-149. <https://doi.org/10.1016/j.jafrearsci.2016.03.009>
- [38] Yousefi, M., Kamkar-Rouhani, A. and Carranza, E.J.M. (2014). Application of staged factor analysis and logistic function to create a fuzzy stream sediment geochemical evidence layer for mineral prospectivity mapping. *Geochemistry: Exploration, Environment, Analysis*, 14(1), 45-58. <https://doi.org/10.1144/geochem2012-144>
- [39] Saremi, M., Maghsoudi, A., Ghezlbash, R., Yousefi, M. and Hezarkhani, A. (2024). Targeting of porphyry copper mineralization using a continuous-based logistic function approach in the Varzaghan district, north of Urumieh-Dokhtar magmatic arc. *Journal of Mining and Environment*,
- [40] Saremi, M., Yousefi, S. and Yousefi, M. (2023). Separation of geochemical anomalies related to

hydrothermal copper mineralization using staged factor analysis in Feizabad geological map. *Journal of Analytical and Numerical Methods in Mining Engineering*, 14 (38), 35–44.

[41] Saremi, M., Hoseinzade, Z., Mirzabozorg, S.A.A.S., Pour, A.B., Zoheir, B. and Almasi, A. (2024). Integrated remote sensing and geochemical studies for enhanced prospectivity mapping of porphyry copper deposits: A case study from the Pariz district, Urmia-Dokhtar metallogenic belt, southern Iran. *Remote Sensing Applications: Society and Environment*, Elsevier, 36, 101343. <https://doi.org/10.1016/J.RSASE.2024.101343>

[42] Yousefi, M. and Carranza, E.J.M. (2015). Prediction-area (P-A) plot and C-A fractal analysis to classify and evaluate evidential maps for mineral prospectivity modeling. *Computers and Geosciences*, 79, 69-81. <https://doi.org/10.1016/j.cageo.2015.03.007>

[43] Mokhtari, M., Hoseinzade, Z. and Shirani, K. (2020). A comparison study on landslide prediction through FAHP and Dempster–Shafer methods and their evaluation by P–A plots. *Environmental Earth Sciences*, 79, 1-13. <https://doi.org/10.1007/s12665-019-8804-0>

[44] Hoseinzade, Z., Zavarei, A. and Shirani, K. (2021). Application of prediction–area plot in the assessment of MCDM methods through VIKOR, PROMETHEE II, and permutation. *Natural Hazards*, 109, 2489-2507. <https://doi.org/10.1007/s11069-021-04929-w>

[45] Saremi, M., Yousefi, S. and Yousefi, M. (2024). Combination of geochemical and structural data to determine the exploration target of copper hydrothermal deposits in the Feizabad district. *Journal of Mining and Environment*, 15(3), 1089-1101.

[46] Saremi, M., Maghsoudi, A., Hoseinzade, Z. and Mokhtari, A.R. (2024). Data-driven AHP: a novel method for porphyry copper prospectivity mapping in the Varzaghan District, NW Iran. *Earth Science Informatics, Springer Science and Business Media Deutschland GmbH*, 1–16. <https://doi.org/10.1007/S12145-024-01481-6/METRICS>

[47] Huang, D., Zuo, R. and Wang, J. (2022). Geochemical anomaly identification and uncertainty quantification using a Bayesian convolutional neural network model. *Applied Geochemistry*, 146, 105450. <https://doi.org/10.1016/j.apgeochem.2022.105450>

[48] Wang, J. and Zuo, R. (2022). Model averaging for identification of geochemical anomalies linked to mineralization. *Ore Geology Reviews*, 146, 104955. <https://doi.org/10.1016/j.oregeorev.2022.104955>

[49] Yousefi, M., Lindsay, M.D. and Kreuzer, O. (2024). Mitigating uncertainties in mineral exploration targeting: Majority voting and confidence index approaches in the context of an exploration information system (EIS). *Ore Geology Reviews*, 105930. <https://doi.org/10.1016/j.oregeorev.2024.105930>

[50]. Ihara, C. K. (1981). Maximin and other decision principles. *Philosophical topics*, 12(3), 59-72.



دانشگاه صنعتی شاهرود

# نشریه مهندسی معدن و محیط زیست

www.jme.shahroodut.ac.ir نشانی نشریه:



انجمن مهندسی معدن ایران

## به کارگیری روش نقشه خودسازمان دهی عمیق-تعبیه شده به منظور شناسایی آنومالی های ژئوشیمیایی در منطقه معلمان، ایران

زهره حسین زاده و محمد حسن بازوبندی\*

گروه آموزش علوم تجربی، دانشگاه فرهنگیان، صندوق پستی ۱۴۶۶۵۸۸۹ تهران، ایران

| چکیده  | اطلاعات مقاله   |
|--|---|
| <p>تشخیص ناهنجاری به معنای یافتن الگوهایی در داده‌ها است که با رفتار معمول و مورد انتظار سازگاری ندارند. در زمینه ژئوشیمی، این موضوع به شناسایی الگوهای پنهان و غیرمعمول در فرایند شناسایی تارگت‌های اکتشافی مربوط می‌شود. این مسئله به‌ویژه زمانی اهمیت پیدا می‌کند که اطلاعات اندکی از منطقه مورد نظر در دسترس باشد. بنابراین، استفاده از روش‌هایی که بتوانند در چنین شرایطی و با وجود محدودیت‌های اطلاعاتی، به فرایند اکتشاف کمک کنند، بسیار ارزشمند است. در این پژوهش، از روش یادگیری عمیق بدون نظارت موسوم به نقشه خودسازمانده عمیق-تعبیه شده به منظور شناسایی ناهنجاری‌های ژئوشیمیایی استفاده شد. این پژوهش بر شناسایی ناهنجاری‌های ژئوشیمیایی چندمتغیره در منطقه معلمان تمرکز داشت. پس از شناسایی ناهنجاری‌های ژئوشیمیایی منطقه، کارایی الگوریتم در کنار دو نوع دیگر از الگوریتم‌های نقشه خود سازمانده ارزیابی شد. برای این منظور، از نمودار نرخ پیش‌بینی-مساحت استفاده گردید و نقاط تقاطع برای نقشه خودسازمانده عمیق-تعبیه شده، نقشه خود سازمانده دسته‌ای و نقشه خود سازمانده به ترتیب ۰.۷۵، ۰.۶۷ و ۰.۶۵ تعیین شدند. ناهنجاری ژئوشیمیایی چندمتغیره در منطقه معلمان ارتباط خوبی با رخداد‌های معدنی شناخته شده و واحدهای آندزیت و داسیت نشان می‌دهد. بر این اساس، می‌توان بیان کرد که روش نقشه خودسازمانده عمیق-تعبیه شده ابزار مفیدی برای شناسایی ناهنجاری‌ها و الگوهای مرتبط با کانی‌سازی است.</p> | <p><b>تاریخ ارسال:</b> ۲۰۲۴/۰۹/۰۳<br/> <b>تاریخ داور:</b> ۲۰۲۴/۰۹/۱۸<br/> <b>تاریخ پذیرش:</b> ۲۰۲۴/۱۱/۰۸</p> <p>DOI: 10.22044/jme.2024.15003.2861</p> <p><b>کلمات کلیدی</b></p> <p>گالری اصلی<br/> ناحیه آسیب‌دیده حفاری<br/> کارگاه استخراج جبهه کار طولانی<br/> ناحیه تخریب<br/> مدل هندسی جدید</p> |